The Role of Subslab Low-Velocity Anomalies Beneath the Nazca Ridge and Iquique Ridge on the Nazca Plate and Their Possible Contribution to the Subduction Angle

Hwaju Lee[1,2] , YoungHee Kim[1,2] , Maximiliano J. Bezada[3] , and Robert W. Clayton[4]

[1]Research Center for Deep-Surface Coupling of Earth, Seoul, Republic of Korea, [2]School of Earth and Environmental Sciences, Seoul National University, Seoul, Republic of Korea, [3]Department of Earth and Environmental Sciences, University of Minnesota, Minneapolis, MN, USA, [4]Division of Geological and Planetary Sciences, California Institute of Technology, Pasadena, CA, USA

Abstract Subducting the buoyant crustal material of an aseismic oceanic ridge has been regarded as a dominant contributor to flat slab subduction. However, normal-dip subduction is also observed in some cases where ridges are subducting. In this study, we compare the subduction of two ridges on the Nazca Plate: Nazca Ridge (flat slab) and Iquique Ridge (normal-dip slab). Anisotropy determined by shear wave splitting observation suggests that the low-velocity anomalies found beneath the ridges are mapping anisotropic structure into isotropic velocities. After a tomographic inversion incorporating anisotropy models for both ridges, we find that the low-velocity anomalies found beneath the Nazca Ridge are not anisotropic and therefore likely represent warm mantle, and those beneath the Iquique Ridge are caused by anisotropy. We conclude that subslab mantle buoyancy has a larger impact on the subduction angle than the crustal material of the ridge.

Plain Language Summary Understanding the subduction process and how the mantle flows is pivotal in understanding the planetary evolution of Earth. Yet, several subduction characteristics remain unsolved, and the angle of plate subduction, which is often categorized into <30° (shallow), ~30–35° (normal), >35° (steep), is one of those. Subduction of an oceanic ridge on a plate has been proposed as a cause of a shallow subduction angle since the thick crust of the ridge is less dense than the surrounding mantle. However, normal angles have been observed in some cases where oceanic ridges are subducting. In this study, we compare the Nazca Ridge and the Iquique Ridge, on the Nazca Plate subducting beneath South America. The subduction angles of the Nazca and Iquique Ridges are shallow and normal, respectively. When we incorporate directional variations in seismic wave velocities, which are produced by mantle flow, in seismic tomographic imaging, we find that the subducting oceanic ridge may not be a primary factor producing shallow angle subduction. Instead, the warm mantle beneath the Nazca Ridge may provide the buoyancy to support the Nazca Plate. Comparably, since the mantle beneath the Iquique Ridge is not warm, the subduction angle would stay normal.

1. Introduction

The subduction of an aseismic oceanic ridge has been considered one of the key factors that leads to low-angle subduction as the thick crust of the ridge should contribute to the buoyancy of the slab (e.g., Espurt et al., 2008; Schellart, 2020). On the Nazca Plate in South America, two prominent flat subduction segments (Peruvian and Pampean flat subduction zones) are spatially correlated with the subduction of the Nazca Ridge and Juan Fernandez Ridge, respectively (Gutscher et al., 2000; Pilger, 1981; van Hunen et al., 2004). However, in the same subduction system, the subduction of a ridge occurs with normal subduction angles (~30–35°) (Iquique Ridge and Carnegie Ridge at Nazca (Espurt et al., 2008; Guillier et al., 2001; Schellart, 2020; Skinner & Clayton, 2013)). In fact, other subduction zones like the case of the central Mexico subduction zone (Kim et al., 2010, 2013) show that flat subduction does not require the presence of a ridge. Previous studies have suggested several other factors that can contribute to the slab flattening process such as (a) the thickness of the overriding plate (e.g., Holt et al., 2015; Horton et al., 2022; Manea et al., 2012, 2017; van Hunen et al., 2004), (b) age, temperature, and size of the subduction zone (e.g., English et al., 2003; Protti et al., 1995; Schellart, 2020), (c) mantle plume and/or warm mantle beneath the slab due to slab tears or gaps (Antonijevic et al., 2016; Bishop et al., 2018; Király et al., 2020; Portner et al., 2017; Scire et al., 2016), (d) formation of a low viscosity wedge or a low

Software: Hwaju Lee, Maximiliano J. Bezada
Supervision: YoungHee Kim
Validation: Hwaju Lee
Visualization: Hwaju Lee
Writing – original draft: Hwaju Lee
Writing – review & editing: Hwaju Lee, YoungHee Kim, Maximiliano J. Bezada, Robert W. Clayton

viscosity channel atop the slab (Manea & Gurnis, 2007), and (e) combinations of multiple of these or other factors (Flórez-Rodríguez et al., 2019; Gutscher et al., 2000; Protti et al., 1995; Suchoy et al., 2022).

The Nazca Plate has been a natural laboratory for studying the mechanism affecting subduction angles, which vary along strike, while having multiple aseismic ridges on the subducting plate (Eakin et al., 2014; Espurt et al., 2008; Gutscher et al., 2000; Horton et al., 2022; Kim & Clayton, 2015; Manea et al., 2017; Schellart, 2020; Skinner & Clayton, 2013). Among the ridges on the Nazca Plate, a 200-km-wide Nazca Ridge, was formed at the East Pacific Rise and subducts beneath southern Peru in a shallow-to-horizontal angle (Figure 1a) (Hampel, 2002; Hampel et al., 2004; Pilger, 1981; Pilger & Handschumacher, 1981; Woods & Okal, 1994). Beneath the subducted Nazca Ridge, seismic tomography models show subslab low-velocity anomalies (SSLAs), which indicate a warm and hence more buoyant mantle that could potentially lead to the flat slab subduction (Figures 2a and 2c) (Bishop et al., 2018; Portner et al., 2017; Rodríguez et al., 2021). Roughly ~700 km south of the Nazca Ridge, another SSLA is also imaged with seismic tomography beneath the subducted ~200-km-wide Iquique Ridge (Portner et al., 2020; Scire et al., 2015) (Figures 2e and 2g). This ridge originated at the Foundation Hotspot (Bello-González et al., 2018; Myers et al., 2022), but in this case, the subduction of the ridge does not appear to contribute to the slab flattening (Espurt et al., 2008; Portner et al., 2020; Scire et al., 2016). Intriguingly, although both slab segments include an aseismic ridge and an SSLA, only one of them experiences flat subduction.

Seismic anisotropy is another seismic parameter that may have some bearing on this question. Anisotropy measured by shear wave splitting (SWS) (Deng et al., 2017; Eakin et al., 2014, 2015; Long et al., 2016; Lynner & Beck, 2020; Polet et al., 2000; Reiss et al., 2018) has shown evidence for subduction segments with contrasting mantle geodynamics below two different ridge systems. Good coverage of SWS observation from dense seismic arrays in South America, where the Nazca and Iquique ridges subduct (Figure 1b), allows us to improve the quality of teleseismic tomography by incorporating anisotropy and thus to clarify mantle geodynamic processes (e.g., Bezada et al., 2016; Huang et al., 2019; Lee et al., 2021, 2022; Wang & Zhao, 2012; Zhao et al., 2016). In particular, we can investigate whether SSLAs on isotropic velocity models can be explained by anisotropic structure. When anisotropic structure does not explain the SSLAs, it may indicate that warm and therefore, buoyant mantle would have been imaged as SSLAs that can support shallow subduction angle. In this study, we aim to investigate the SSLAs on the Nazca Plate and their possible role in the subduction angle.

2. Data and Method

2.1. Tomographic Inversion

We inverted 56,364 travel-time delays of teleseismic P waves for our tomography models. The delays came from 507 events that are ≥ magnitude 5.5 within the 30–90° and 155–180° distances (449 direct P and 58 PKIKP phases, respectively) during the 6 years (2007–2013) (Table S1 and Figure S1 in Supporting Information S1). They were recorded by 237 stations in southern Peru, Bolivia, and northern Chile (Figure 1, red inverted triangles). Three bandpass filters (0.3, 0.5, and 1.0 Hz) were used for the manually picked waveforms, and the multi-channel cross-correlation method of VanDecar and Crosson (1990) was applied to obtain travel-time delays. The AK135 velocity model (Kennett et al., 1995) was used for the reference arrival times. To invert the travel-time delays for the tomographic inversion, we adopted the hybrid ray-tracing method of Bezada et al. (2013) that used approximated Born kernels of Schmandt and Humphreys (2010) in addition to the iterative ray tracing. The method assumes 1-D travel times to the outside of the model volume while travel times inside the volume are calculated using a graph theory-based 3-D ray tracer (Hammond & Toomey, 2003; Toomey et al., 1994). For details, we refer to Bezada et al. (2013). To overcome the poor resolution near the top of the model of teleseismic tomography, station terms and crustal corrections are commonly applied to the model. Alternatively, introducing additional pieces of information such as shallow velocity structure can help the poor resolution issue. We used the tomography model of Ward et al. (2013) for the structure <50 km as a starting model, which delivered the shear wave velocity structure of the Central Andes by inverting Rayleigh-wave velocity measurements. We used a constant V_P/V_S ratio of 1.8 used in Schmandt and Humphreys (2010) and Bezada et al. (2013). Based on receiver function analysis, Ryan et al. (2016) have suggested V_P/V_S ratio of 1.75; however, since we remove the mean velocity value for each depth slice during each inversion to image velocity anomalies tuned on relative time delays, the V_P/V_S ratio difference of 0.05 would not be significant. We regularized the inversion by applying damping and smoothing with the preferred values found using the L-curve (the trade-off curve) (Figure S2 in Supporting Information S1). We also applied station and event corrections to remove the near-surface structure
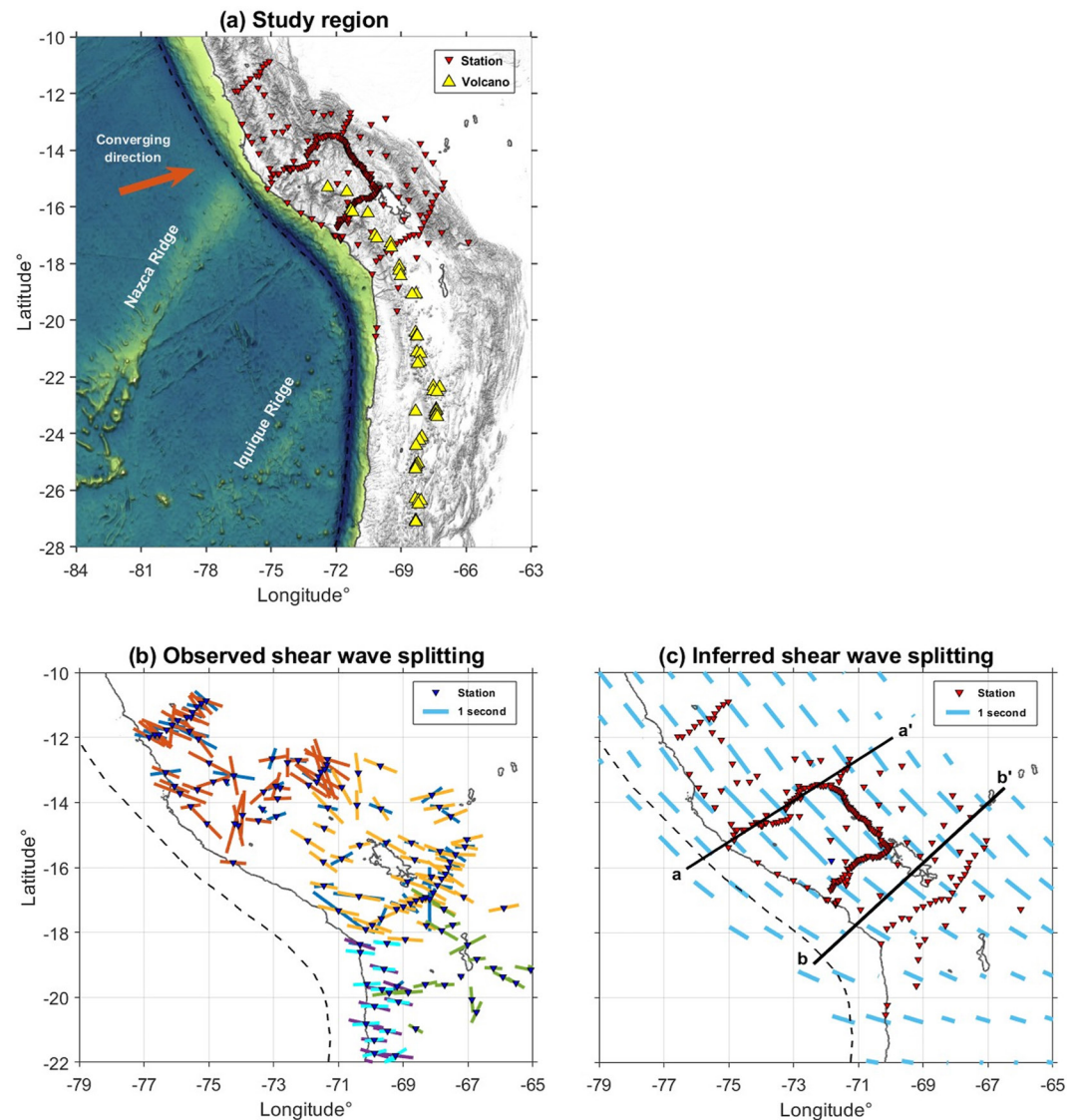
Figure 1. (a) Study region with seismic stations (red inverted triangles) used in this study. Yellow triangles show the location of volcanoes (Syracuse & Abers, 2006). The converging direction (N76°E) of the Nazca plate toward the South America plate is shown in an orange arrow (Norabuena et al., 1998). (b) The navy inverted triangles show shear wave splitting (SWS) stations. Colored bars on the stations show the observed SWS results of Deng et al. (2017) (blue), Eakin et al. (2014, 2015) (orange), Long et al. (2016) (yellow), Lynner and Beck (2020) (purple), Polet et al. (2000) (green), and Reiss et al. (2018) (cyan). (c) Our inferred SWS for the stations used in this study as shown in (a) (red inverted triangle). The black solid lines labeled as a-a′ and b-b′ are the cross-sectional lines that are used in Figure 2. For (b) and (c), the length of the light blue bar represents the SWS time while its orientation represents the fast polarization direction of the inferred SWS.

and event-dependent travel times, respectively. The parameters are kept constant in the inversion. We have carried out various synthetic tests to ensure the robustness of the tomographic inversion (Figures S3 and S4 in Supporting Information S1).

2.2. Anisotropy in Isotropic Tomography

Since introducing anisotropy in the tomographic inversion increases the non-uniqueness effect in the inversion, tomographic inversion is often kept as isotropic despite it being well known that the mantle is seismically anisotropic. In this study, we take a hypothesis-testing approach and carry out the isotropic inversion with anisotropy-corrected travel-time delays. For the correction, we removed the travel-time delays imposed
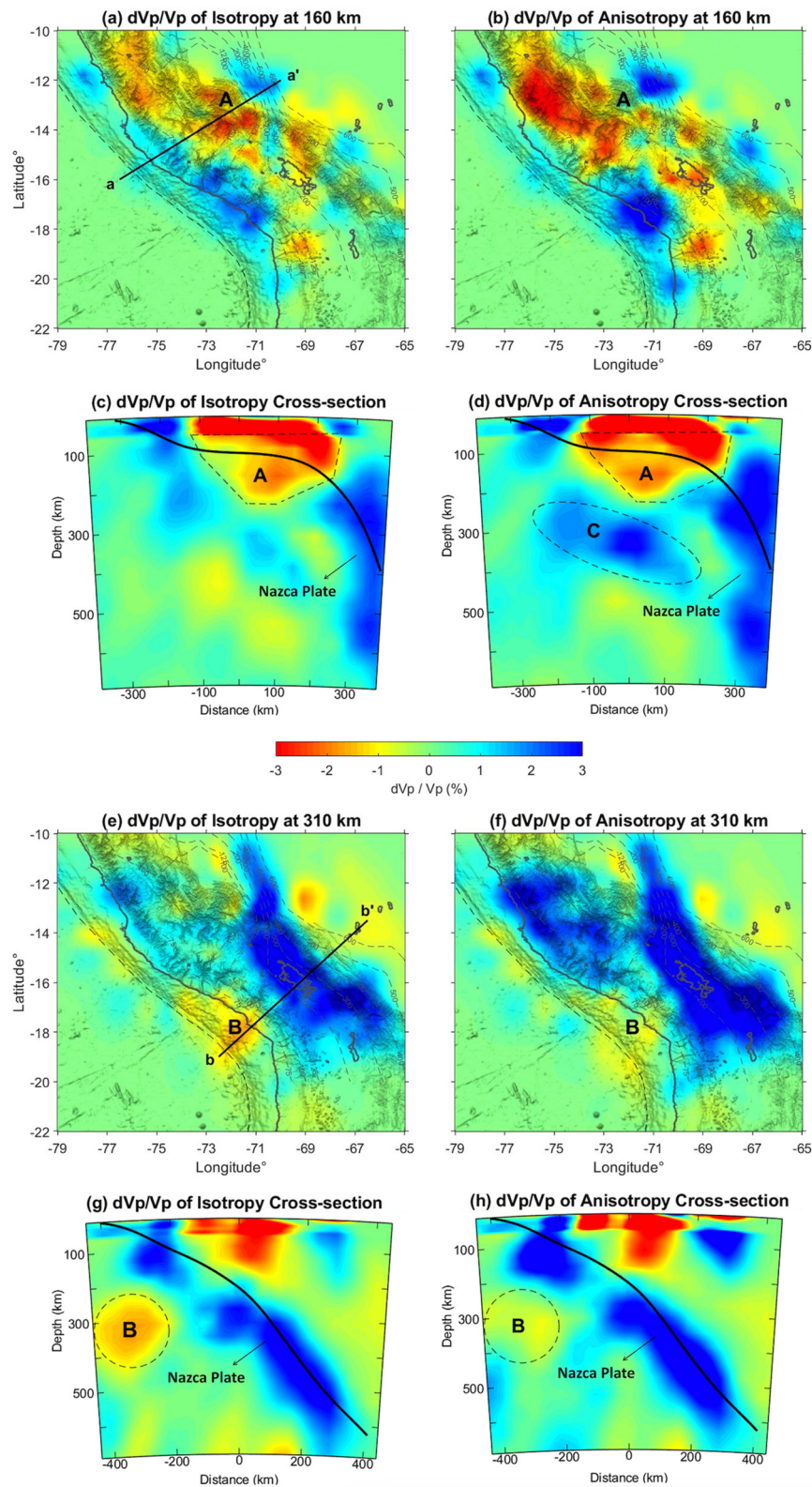
Figure 2.

by the field of hypothetical anisotropy structure during the forward travel-time calculation before inverting for isotropic velocity perturbations (Hammond & Toomey, 2003). The hypothetical anisotropy field was derived from SWS observations (Deng et al., 2017; Eakin et al., 2014, 2015; Long et al., 2016; Lynner & Beck, 2020; Polet et al., 2000; Reiss et al., 2018) and it is constant throughout each iteration. Further details about our alternative method can be found in Bezada et al. (2016) and Lee et al. (2021, 2022). Unaccounted-for anisotropy can produce artificial velocity anomalies in isotropic tomography that can be misleading (Bezada et al., 2016; Blackman & Kendall, 1997; Eberhart-Phillips & Henderson, 2004; Ishise & Oda, 2005; Lee et al., 2021; Lloyd & Van der Lee, 2008; Menke, 2015; Sobolev et al., 1999; VanderBeek & Faccenda, 2021). Consequently, tomographic inversion with an appropriate approximate anisotropy structure would reduce artifacts and result in a smaller model norm. Conversely, we expect increases in the model norm when hypothetical anisotropy structures are not a good representation of true mantle anisotropy, as we expect additional velocity artifacts to be produced.

2.3. Anisotropy Models From SSLAs and SWS Observations

Previous studies have suggested the development of mantle flow-derived anisotropy occurs beneath subducting slabs (Currie et al., 2004; Di Leo et al., 2012; Faccenda & Capitanio, 2012, 2013; Fouch & Fischer, 1996). In the Nazca subduction zone, the SWS observations in our study region (Deng et al., 2017; Eakin et al., 2014, 2015; Long et al., 2016; Lynner & Beck, 2020; Polet et al., 2000; Reiss et al., 2018) are a result of upper mantle anisotropy, indicating mantle flow complexities. When the seismically fast axis of anisotropy (e.g., a-axis of A-type olivine) is aligned sub-horizontally, which is perpendicular to the propagating direction of seismic wave, seismic velocity would decrease and be mapped as low-velocity anomalies (Bezada et al., 2016; Blackman & Kendall, 1997; Eberhart-Phillips & Henderson, 2004; Ishise & Oda, 2005; Lee et al., 2021; Lloyd & Van der Lee, 2008; Menke, 2015; Sobolev et al., 1999; VanderBeek & Faccenda, 2021). We, therefore, explore the hypothesis that the SSLAs found beneath the Nazca Plate where the Nazca and Iquique ridges are subducting solely come from the ignored anisotropy in isotropic tomography models. Consequently, the volume and shape of anisotropic regions in our model are the same as the volume and shape of SSLAs. To incorporate the anisotropy structure in the tomographic inversion, we derived two anisotropy models: one for the Nazca Ridge and the other one for Iquique Ridge based on the observations of SWS (Figure 1 and Figure S6 in Supporting Information S1) (Deng et al., 2017; Eakin et al., 2014, 2015; Long et al., 2016; Lynner & Beck, 2020; Polet et al., 2000; Reiss et al., 2018). To determine the effect of the prescribed anisotropy model for each targeting SSLA independently, two anisotropy models went through the inversion separately. Further details on developing seismic anisotropy models from SWS such as converting SWS time to an anisotropic field are found in Text S1 and Figure S6 of Supporting Information S1.

3. Results

3.1. Isotropic Tomography

3.1.1. Nazca Ridge

As previous tomographic studies have found (Bianchi et al., 2013; Gutscher et al., 2000; Portner et al., 2017; Rodríguez et al., 2021; Scire et al., 2016), we image a flat slab structure (Figures 2a and 2c, denoted as "Nazca Plate") beneath the Nazca Ridge as well as SSLAs from the isotropic tomography (Figures 2a and 2c, denoted as "A"). The low-velocity anomalies extend from the top to ~200 km depth (Figure 2 and Figure S7 in Supporting Information S1).

3.1.2. Iquique Ridge

We find other low-velocity anomalies (Figures 2e and 2g, denoted as "B") beneath the Nazca Plate where Iquique Ridge subducts at a normal angle (Figures 2e and 2g, denoted as "Nazca Plate"). The low-velocity anomalies

Figure 2. (a) Isotropic and (b) prescribed anisotropy tomography slices at 160 km showing targeted sub-slab low-velocity anomalies beneath the Nazca Ridge denoted as "A." Cross-sectional views of (c) isotropic and (d) prescribed anisotropy tomographies along the profile a-a′ in (a). High-velocity anomalies denoted as "C" in only (d) show possible artifact velocity anomalies from considering inappropriate anisotropy structure for sub-slab low-velocity anomalies beneath the Nazca Ridge. (e) Isotropic and (f) prescribed anisotropy tomography slices at 310 km showing targeted sub-slab low-velocity anomalies beneath the Iquique Ridge denoted as "B." Cross-sectional views of (g) isotropic and (h) prescribed anisotropy tomographies along the b-b′ in (e). The thick dashed gray line in (a), (b), (e), and (f) shows the trench while thin dashed gray lines show the iso-depth contours of the subducted Nazca Plate by Scire et al. (2016). The solid black line in (c), (d), (g), and (h) shows the slab contour suggested by Slab2 of Hayes et al. (2018).

beneath the Iquique Ridge are distributed at a depth of 250–420 km in the isotropic tomography (Figure 2g). High-velocity structures in our isotropic tomography images (Figure 2 and Figure S8 in Supporting Information S1), which represent the subducted Nazca Plate, are generally consistent with the slab contour line suggested by Slab2 of Hayes et al. (2018).

3.2. Tomography With Prescribed Anisotropy

3.2.1. Nazca Ridge

When we have prescribed anisotropy for Nazca Ridge in the tomographic inversion, we do not find a decrease in low-velocity anomalies (Figures 2b and 2d). Instead, we do find an increase in the volume of low-velocity anomalies. Incorporating the anisotropy model in the inversion introduced high-velocity anomalies beneath the targeted low-velocity anomalies at 250–420 km (Figure 2d, denoted as "C"). Consequently, the model norm has increased by ~50% from the isotropic tomography to the prescribed anisotropy tomography while the travel time residuals stay constant (~0.34 s in both cases, Figure S9 in Supporting Information S1).

3.2.2. Iquique Ridge

In contrast to the Nazca Ridge, we find a reduction in targeted low-velocity anomalies (~1.5% dV_P/V_P) when the hypothetical anisotropy model for the Iquique Ridge is prescribed in the inversion (Figures 2f and 2h). In addition, the intensity of the high-velocity structure, which represents the subducted Nazca Plate, increased by ~1% dV_P/V_P compared to the isotropic tomography result (Figures 2e–2h) and the model norm has decreased by ~25% (Figure S9 in Supporting Information S1). Similarly, the travel time residuals do not change substantially for the Iquique Ridge region. The travel time residuals of isotropic and prescribed anisotropic models for depths 250–420 km are ~0.40 and ~0.39 s, respectively.

4. Discussion

When we incorporate hypothetical anisotropy in the tomographic inversion to investigate the origin of the low-velocity anomalies and their possible role in subduction geometry, we find an increase in low-velocity anomalies for the SSLAs beneath the Nazca Ridge. In contrast, we find a velocity reduction of ~1.5% dV_P/V_P in the SSLAs beneath the Iquique Ridge compared to the isotropic tomography (Figure 2). When the prescribed anisotropy in the inversion is not a good approximation of true mantle anisotropy, it may introduce additional artificial velocity structure and therefore lead to an increase in the model norm (Figure S9 in Supporting Information S1) (Bezada et al., 2016; Lee et al., 2021, 2022).

4.1. Subslab Low-Velocity Anomalies Below Nazca Ridge

Our result suggests that the SSLAs found beneath the Nazca Ridge may not be due to anisotropy. When hypothetical anisotropy was prescribed in the inversion, the targeted low-velocity anomalies were increased in terms of magnitude and spatial distribution, and additional high-velocity anomalies were introduced (Figures 2a–2d and Figure S6 in Supporting Information S1). This led to an increase in the model norm (Figure S9 in Supporting Information S1). One of the other candidates that could decrease seismic velocity is a warm and/or hydrous mantle. It has been already suggested by several previous studies that the SSLAs found beneath the Nazca Ridge could come from a warm mantle which may provide buoyancy to the Nazca Plate (Bishop et al., 2018; Király et al., 2020; Portner et al., 2017; Scire et al., 2016). For instance, with receiver function analysis, Bishop et al. (2018) have suggested that the base of the crust beneath the Nazca Ridge has been extensively eclogitized at ~350 km from the trench, which would need other mechanisms to support the flat slab angle. They argue that warm mantle, which would be imaged as SSLAs in tomography, is one of the likely mechanisms of slab flattening. Once the slab flattens, suction forces may play an important role in maintaining the flat slab geometry in the vicinity of the subducting ridge (Kim & Clayton, 2015; Ma & Clayton, 2015). The constriction of the mantle layer between the flat slab and continental crust inhibits typical asthenospheric corner flow, leading to a large negative pressure that further decreases the dip angle of the slab (Ma & Clayton, 2015) as well as a decrease in the degree of partial melting of the mantle at the volcanic arc.

We have converted the low-velocity anomalies found beneath the Nazca Ridge of the Nazca Plate from the isotropic tomography into temperature based on the temperature derivatives of P-wave velocity at 160 km

(Cammarano et al., 2003) (Figure 3a). For the conversion, we assume that the pressure is ~5 GPa (i.e., 1 GPa for every 30 km), and the dry solidus of mantle rock is ~1650°C at 160 km depths (Hirschmann, 2000). Our approximation of temperature conversion indicates that melt may be present in the mantle below the Nazca Ridge (>1800°C) (Figures 3a, 3b, and 3e). Considering mantle plume has 100–300°C of excessive temperature than the surrounding mantle (Anderson & Natland, 2007; Bao et al., 2022; Herzberg et al., 2007; Herzberg & O'Hara, 2002; McKenzie & O'Nions, 1991; Putirka, 2005; Schilling, 1991), a temperature difference of ~150°C (between 1650°C and 1800°C) is significantly warm for subduction setting. For comparison, we have converted the dV_P/V_P from the prescribed anisotropy velocity model into temperature (Figure 3b). As incorporating anisotropy in the tomographic inversion introduced extra low-velocity anomalies in the model, we find higher temperatures from anisotropic tomography slice at a depth of 160 km (up to ~300°C higher than the isotropic result). As mentioned above, we conclude that the SSLAs may not come from seismic anisotropy. This exemplifies that introducing inappropriate anisotropy structure can mislead the interpretations of mantle dynamics based on tomography.

Based on our results only, it is still difficult to suggest the origin of the SSLAs (Figure 2a). Perhaps, it comes from hosting hotspot tracks as Contreras-Reyes et al. (2019) observed buoyant over-thicked lower crust as a feature of hotspot tracks based on joint refracting and reflection traveltime tomographic studies. Although our results could eliminate anisotropy as a possible origin for the SSLAs, further studies on mantle temperature and consequent buoyancy, as well as mantle flow dynamics of the region, are necessary to understand the relationship between low-velocity anomalies and subduction angle.

In our models, dipping segments of the slab are well recovered as high-velocity features from our inversion whereas the flat slab segment is not (Figure S3 in Supporting Information S1). The flat slab segment is well recovered with high velocities from local double-difference tomography (Lim et al., 2018) and surface wave tomography studies (Antonijevic et al., 2015; Ward et al., 2016) as well as low seismic attenuation from local earthquake data (Jang et al., 2019). Our synthetic tests for the Nazca Ridge show a gap in the slab that may appear as low-velocity anomalies in the inversion (Figure S3 in Supporting Information S1). We note that seismic ray coverage is relatively abundant given station geometries (Figure 1a), and the inversions of low-velocity anomalies for the flat slab segment do recover low-velocity anomalies (Figure S3 in Supporting Information S1).

4.2. Subslab Low-Velocity Anomalies Below Iquique Ridge

In contrast to Nazca Ridge, the reduction of SSLAs (~1.5% dV_P/V_P; Figures 2e–2h and Figure S7 in Supporting Information S1), as well as the model norm (~25%; Figure S9 in Supporting Information S1), under Iquique Ridge, indicates that the imaged low-velocity anomalies in the isotropic tomography at depths of 250–420 km may be the product of seismic anisotropy rather than warm and/or hydrous mantle. We have estimated the temperature at 310 km depth based on our isotropic and anisotropic tomographic results (Figures 3c and 3d). The solidus at 310 km (~10 GPa) is ~1900°C (Hirschmann, 2000), and, therefore, melt would be likely present beneath the Iquique Ridge as the approximated temperature of isotropic tomography is over 2000°C (Figure 3c). In other words, the isotropic tomography model suggests that the mantle beneath the Iquique Ridge is warm. However, the estimated temperature based on prescribed anisotropy tomography implies that the melt is not necessarily to be present beneath the ridge as the estimated temperature is ~1900°C (Figures 3d and 3e). This follows the result beneath the Nazca Ridge (Section 4.1). The SSLAs from anisotropy do not provide any buoyancy to the slab, which is more consistent with the normal subduction angle of the Nazca Plate beneath the Iquique Ridge (Figure 2). Our results show that considering anisotropy provides useful constraints for understanding subduction mechanisms in addition to other significant factors such as the age of the plate, slab temperature as well as surrounding mantle temperature, subduction velocity, slab composition, properties of the overriding plate, and hydrous status influence the subduction geometry (English et al., 2003; Flórez-Rodríguez et al., 2019; Gutscher et al., 2000; Manea et al., 2017; Martinod et al., 2005; Skinner & Clayton, 2013; van Hunen et al., 2004).

Since our result suggests that SSLAs beneath the Iquique Ridge may come from the anisotropic mantle (Figures 2e–2h; Figures S6c, S6d, and S8 in Supporting Information S1), our approximation of mantle anisotropy based on SWS observation is acceptable beneath the Iquique Ridge. As the fast polarization direction of SWS can represent the direction of mantle flow and it is generally trench parallel, our prescribed anisotropy tomography suggest that the slab beneath the Iquique Ridge may not have any tears or holes. If they did exist, mantle flow would go through, which would be observed as trench-perpendicular fast polarization direction of
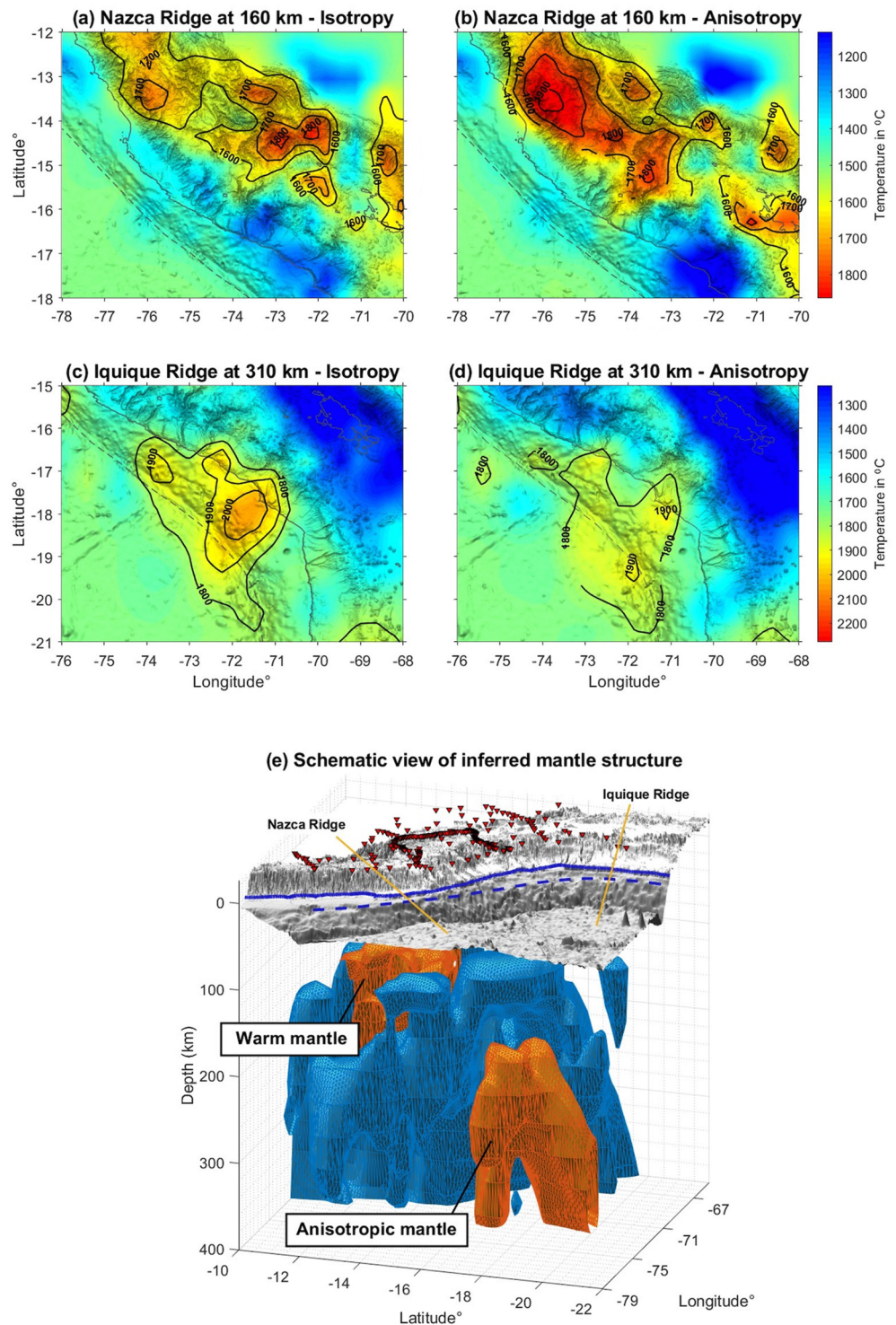
Figure 3. Estimated mantle temperature for the sub-slab low-velocity anomalies of (a) isotropic and (b) prescribed anisotropy tomographies beneath the Nazca Ridge based on the 160-km-depth slice (same temperature color bar); (c) isotropic and (d) prescribed anisotropy tomographies beneath the Iquique Ridge based on the 310-km-depth slice (same temperature color bar). The temperature contour is indicated in black. (e) A schematic view of inferred mantle structure for sub-slab low-velocity anomalies beneath the Nazca Plate. The blue structure represents high-velocity anomalies that may show slab structure while the orange structure represents low-velocity anomalies. The navy solid and dashed lines on the topography present coastal and trench lines, respectively. Our study suggests that subslab low-velocity anomalies found beneath the Nazca Ridge and Iquique Ridge come from warm temperatures and anisotropic mantle, respectively.

SWS. Further south (>latitude 20⁰ south; Figure 1b), the observed SWS changes to trench-perpendicular. It has been understood as the presence of a stagnation point of the Nazca Plate that led mantle flow to be well coupled with the Nazca Plate (e.g., Lynner & Beck, 2020; Reiss et al., 2018; Russo & Silver, 1994). We would also expect trench-perpendicular fast polarization direction of SWS when the mantle is strongly entrained with the subduction slab (Currie et al., 2004; Di Leo et al., 2012; Eakin et al., 2015, 2015, 2015; Faccenda & Capitanio, 2012, 2013; Fouch & Fischer, 1996; Long, 2016; Long & Becker, 2010; Savage, 1999). Our results show that the mantle at the targeted depths (250–420 km) beneath the Iquique Ridge may not be strongly coupled with the subducting Nazca Plate. The seismically fast direction of other olivine fabrics is different than A-type fabric (e.g., Ismaïl & Mainprice, 1998; Jung & Karato, 2001; Zhang & Karato, 1995). Although further studies on rock and mineral physics need to be carried out, we find that the lattice-preferred orientation of other types of olivine fabric (B-, C-, and E-types) may not be the source of seismic anisotropy, as subslab mantle would be poor in water content and lower in stress compared to the mantle above the slab (Hacker et al., 2003; Jung & Karato, 2001; Jung et al., 2006). We note that our study does not demonstrate that the mantle other than the depth slices that we placed in our anisotropy model is purely isotropic. Rather than determining how anisotropic the mantle is, our study is more focused on exploring tomographic artifacts by ignoring anisotropy and its possible contribution to the subduction dynamics.

5. Conclusions

The main parameters controlling mantle dynamics and subduction geometry remain poorly understood. In this study, taking advantage of dense seismic coverage in southern Peru, Bolivia, and northern Chile, we perform tele-seismic tomography to provide seismic properties of the subducting Nazca Plate where its along-strike geometry varies from flat to normal. Such variations in geometry have been attributed to the subduction of aseismic ridges, notably Nazca Ridge and Iquique Ridge, leading to flat and normal subduction, respectively, while SSLAs are imaged in seismic tomography models beneath the two ridges. As (a) a good coverage of SWS observations offers constraints on seismic anisotropy in the vicinity of two ridges that are subducting, and (b) in isotropic tomography models, low-velocity anomalies can be caused by anisotropy in addition to a warm and hydrous mantle, we incorporate seismic anisotropy in the tomographic inversion that is inferred by the SWS observation. Our results show that the SSLAs found beneath the Nazca Ridge are not related to anisotropy. It may be instead caused by a warm mantle, which suggests that the buoyancy of the slab may be in part controlled by temperature. In contrast, the subslab low-velocity found beneath the Iquique Ridge may be a tomographic image of seismic anisotropy that may not provide any buoyancy to the slab.

Data Availability Statement

Teleseismic data used in this study are accessible through Incorporated Research Institutions for Seismology (IRIS) and GEOFON of GFZ German Research Centre for Geosciences. The data on SWS are obtained from Deng et al. (2017), Eakin et al. (2014, 2015), Long et al. (2016), Lynner and Beck (2020), Polet et al. (2000), and Reiss et al. (2018). MATLAB codes are used to process data (Toomey & Blue Tech Seismics, Inc, 2012) and create figures. The ambient noise tomography model of Ward et al. (2013) was retrieved from the IRIS Earth Model Collaboration. The dV_P/V_P of our prescribed anisotropy tomography model is available online (Lee et al., 2023).

References

Anderson, D. L., & Natland, J. H. (2007). Evidence for mantle plumes? *Nature*, *450*(7169), E15. https://doi.org/10.1038/nature06376

Antonijevic, S. K., Wagner, L. S., Beck, S. L., Long, M. D., Zandt, G., & Tavera, H. (2016). Effects of change in slab geometry on the mantle flow and slab fabric in Southern Peru. *Journal of Geophysical Research: Solid Earth*, *121*(10), 7252–7270. https://doi.org/10.1002/2016JB013064

Antonijevic, S. K., Wagner, L. S., Kumar, A., Beck, S. L., Long, M. D., Zandt, G., et al. (2015). The role of ridges in the formation and longevity of flat slabs. *Nature*, *524*(7564), 212–215. https://doi.org/10.1038/nature14648

Bao, X., Lithgow-Bertelloni, C. R., Jackson, M. G., & Romanowicz, B. (2022). On the relative temperatures of Earth's volcanic hotspots and mid-ocean ridges. *Science*, *375*(6576), 57–61. https://doi.org/10.1126/science.abj8944

Bello-González, J. P., Contreras-Reyes, E., & Arriagada, C. (2018). Predicted path for hotspot tracks off South America since Paleocene times: Tectonic implications of ridge-trench collision along the Andean margin. *Gondwana Research*, *64*, 216–234. https://doi.org/10.1016/j.gr.2018.07.008

Bezada, M. J., Faccenda, M., & Toomey, D. R. (2016). Representing anisotropic subduction zones with isotropic velocity models: A characterization of the problem and some steps on a possible path forward. *Geochemistry, Geophysics, Geosystems*, *17*(8), 3164–3189. https://doi.org/10.1002/2016GC006507

Bezada, M. J., Humphreys, E. D., Toomey, D. R., Harnafi, M., Dávila, J. M., & Gallart, J. (2013). Evidence for slab rollback in westernmost Mediterranean from improved upper mantle imaging. *Earth and Planetary Science Letters*, *368*, 51–60. https://doi.org/10.1016/j.epsl.2013.02.024

Bianchi, M., Heit, B., Jakovlev, A., Yuan, X., Kay, S. M., Sandvol, E., et al. (2013). Teleseismic tomography of the southern Puna plateau in Argentina and adjacent regions. *Tectonophysics*, *586*, 65–83. https://doi.org/10.1016/j.tecto.2012.11.016

Bishop, B. T., Beck, S. L., Zandt, G., Wagner, L. S., Long, M. D., & Tavera, H. (2018). Foreland uplift during flat subduction: Insights from the Peruvian Andes and Fitzcarrald Arch. *Tectonophysics*, *731–732*, 73–84. https://doi.org/10.1016/j.tecto.2018.03.005

Blackman, D. K., & Kendall, J.-M. (1997). Sensitivity of teleseismic body waves to mineral texture and melt in the mantle beneath a mid–ocean ridge. *Philosophical Transactions of the Royal Society of London. Series A: Mathematical, Physical and Engineering Sciences*, *355*(1723), 217–231. https://doi.org/10.1098/rsta.1997.0007

Cammarano, F., Goes, S., Vacher, P., & Giardini, D. (2003). Inferring upper-mantle temperatures from seismic velocities. *Physics of the Earth and Planetary Interiors*, *138*(3), 197–222. https://doi.org/10.1016/S0031-9201(03)00156-0

Contreras-Reyes, E., Muñoz-Linford, P., Cortés-Rivas, V., Bello-González, J. P., Ruiz, J. A., & Krabbenhoeft, A. (2019). Structure of the collision zone between the Nazca Ridge and the Peruvian convergent margin: Geodynamic and seismotectonic implications. *Tectonics*, *38*(9), 3416–3435. https://doi.org/10.1029/2019TC005637

Currie, C. A., Cassidy, J. F., Hyndman, R. D., & Bostock, M. G. (2004). Shear wave anisotropy beneath the Cascadia subduction zone and western North American craton. *Geophysical Journal International*, *157*(1), 341–353. https://doi.org/10.1111/j.1365-246X.2004.02175.x

Deng, J., Long, M. D., Creasy, N., Wagner, L., Beck, S., Zandt, G., et al. (2017). Lowermost mantle anisotropy near the eastern edge of the Pacific LLSVP: Constraints from SKS–SKKS splitting intensity measurements [Dataset]. Geophysical Journal International, *210*(2), 774–786. https://doi.org/10.1093/gji/ggx190

Di Leo, J. F., Wookey, J., Hammond, J. O. S., Kendall, J.-M., Kaneshima, S., Inoue, H., et al. (2012). Deformation and mantle flow beneath the Sangihe subduction zone from seismic anisotropy. *Physics of the Earth and Planetary Interiors*, *194–195*, 38–54. https://doi.org/10.1016/j.pepi.2012.01.008

Eakin, C. M., Long, M. D., Beck, S. L., Wagner, L. S., Tavera, H., & Condori, C. (2014). Response of the mantle to flat slab evolution: Insights from local *S* splitting beneath Peru [Dataset]. Geophysical Research Letters, *41*(10), 3438–3446. https://doi.org/10.1002/2014GL059943

Eakin, C. M., Long, M. D., Wagner, L. S., Beck, S. L., & Tavera, H. (2015). Upper mantle anisotropy beneath Peru from SKS splitting: Constraints on flat slab dynamics and interaction with the Nazca Ridge. [Dataset]. Earth and Planetary Science Letters, *412*, 152–162. https://doi.org/10.1016/j.epsl.2014.12.015

Eberhart-Phillips, D., & Henderson, C. M. (2004). Including anisotropy in 3-D velocity inversion and application to Marlborough, New Zealand. *Geophysical Journal International*, *156*(2), 237–254. https://doi.org/10.1111/j.1365-246X.2003.02044.x

English, J. M., Johnston, S. T., & Wang, K. (2003). Thermal modelling of the Laramide orogeny: Testing the flat-slab subduction hypothesis. *Earth and Planetary Science Letters*, *214*(3), 619–632. https://doi.org/10.1016/S0012-821X(03)00399-6

Espurt, N., Funiciello, F., Martinod, J., Guillaume, B., Regard, V., Faccenna, C., & Brusset, S. (2008). Flat subduction dynamics and deformation of the South American plate: Insights from analog modeling. *Tectonics*, *27*(3), TC3011. https://doi.org/10.1029/2007TC002175

Faccenda, M., & Capitanio, F. A. (2012). Development of mantle seismic anisotropy during subduction-induced 3-D flow. *Geophysical Research Letters*, *39*(11), L11305. https://doi.org/10.1029/2012GL051988

Faccenda, M., & Capitanio, F. A. (2013). Seismic anisotropy around subduction zones: Insights from three-dimensional modeling of upper mantle deformation and SKS splitting calculations. *Geochemistry, Geophysics, Geosystems*, *14*(1), 243–262. https://doi.org/10.1002/ggge.20055

Flórez-Rodríguez, A. G., Schellart, W. P., & Strak, V. (2019). Impact of aseismic ridges on subduction systems: Insights from analog modeling. *Journal of Geophysical Research: Solid Earth*, *124*(6), 5951–5969. https://doi.org/10.1029/2019JB017488

Fouch, M. J., & Fischer, K. M. (1996). Mantle anisotropy beneath northwest Pacific subduction zones. *Journal of Geophysical Research*, *101*(B7), 15987–16002. https://doi.org/10.1029/96JB00881

Guillier, B., Chatelain, J.-L., Jaillard, É., Yepes, H., Poupinet, G., & Fels, J.-F. (2001). Seismological evidence on the geometry of the Orogenic system in central-northern Ecuador (South America). *Geophysical Research Letters*, *28*(19), 3749–3752. https://doi.org/10.1029/2001GL013257

Gutscher, M.-A., Spakman, W., Bijwaard, H., & Engdahl, E. R. (2000). Geodynamics of flat subduction: Seismicity and tomographic constraints from the Andean margin. *Tectonics*, *19*(5), 814–833. https://doi.org/10.1029/1999TC001152

Hacker, B. R., Peacock, S. M., Abers, G. A., & Holloway, S. D. (2003). Subduction factory 2. Are intermediate-depth earthquakes in subducting slabs linked to metamorphic dehydration reactions? *Journal of Geophysical Research*, *108*(B1), 2030. https://doi.org/10.1029/2001JB001129

Hammond, W. C., & Toomey, D. R. (2003). Seismic velocity anisotropy and heterogeneity beneath the Mantle Electromagnetic and tomography Experiment (MELT) region of the East Pacific Rise from analysis of *P* and *S* body waves. *Journal of Geophysical Research*, *108*(B4), 2176. https://doi.org/10.1029/2002JB001789

Hampel, A. (2002). The migration history of the Nazca Ridge along the Peruvian active margin: A re-evaluation. *Earth and Planetary Science Letters*, *203*(2), 665–679. https://doi.org/10.1016/S0012-821X(02)00859-2

Hampel, A., Kukowski, N., Bialas, J., Huebscher, C., & Heinbockel, R. (2004). Ridge subduction at an erosive margin: The collision zone of the Nazca Ridge in southern Peru. *Journal of Geophysical Research*, *109*(B2), B02101. https://doi.org/10.1029/2003JB002593

Hayes, G., Moore, G., Portner, D., Hearne, M., Flamme, H., Furtney, M., & Smoczyk, G. (2018). Slab2, a comprehensive subduction zone geometry model. *Science*, *362*(6410), eaat4723. https://doi.org/10.1126/science.aat4723

Herzberg, C., Asimow, P. D., Arndt, N., Niu, Y., Lesher, C. M., Fitton, J. G., et al. (2007). Temperatures in ambient mantle and plumes: Constraints from basalts, picrites, and komatiites. *Geochemistry, Geophysics, Geosystems*, *8*(2), Q02006. https://doi.org/10.1029/2006GC001390

Herzberg, C., & O'Hara, M. J. (2002). Plume-associated ultramafic magmas of Phanerozoic age. *Journal of Petrology*, *43*(10), 1857–1883. https://doi.org/10.1093/petrology/43.10.1857

Hirschmann, M. M. (2000). Mantle solidus: Experimental constraints and the effects of peridotite composition. *Geochemistry, Geophysics, Geosystems*, *1*(10), 1042. https://doi.org/10.1029/2000GC000070

Holt, A. F., Buffett, B. A., & Becker, T. W. (2015). Overriding plate thickness control on subducting plate curvature. *Geophysical Research Letters*, *42*(10), 3802–3810. https://doi.org/10.1002/2015GL063834

Horton, B. K., Capaldi, T. N., & Perez, N. D. (2022). The role of flat slab subduction, ridge subduction, and tectonic inheritance in Andean deformation. *Geology*, *50*(9), 1007–1012. https://doi.org/10.1130/G50094.1

Huang, Z., Tilmann, F., Comte, D., & Zhao, D. (2019). P wave azimuthal anisotropic tomography in Northern Chile: Insight into deformation in the subduction zone. *Journal of Geophysical Research: Solid Earth*, *124*(1), 742–765. https://doi.org/10.1029/2018JB016389

Ishise, M., & Oda, H. (2005). Three-dimensional structure of P-wave anisotropy beneath the Tohoku district, northeast Japan. *Journal of Geophysical Research*, *110*(B7), B07304. https://doi.org/10.1029/2004JB003599

Ismäil, W. B., & Mainprice, D. (1998). An olivine fabric database: An overview of upper mantle fabrics and seismic anisotropy. *Tectonophysics*, *296*(1–2), 145–157. https://doi.org/10.1016/S0040-1951(98)00141-3

Jang, H., Kim, Y., Lim, H., & Clayton, R. W. (2019). Seismic attenuation structure of southern Peruvian subduction system. *Tectonophysics*, *771*, 228203. https://doi.org/10.1016/j.tecto.2019.228203

Jung, H., & Karato, S. (2001). Water-induced fabric transitions in olivine. *Science*, *293*(5534), 1460–1463. https://doi.org/10.1126/science.1062235

Jung, H., Katayama, I., Jiang, Z., Hiraga, T., & Karato, S. (2006). Effect of water and stress on the lattice-preferred orientation of olivine. *Tectonophysics*, *421*(1), 1–22. https://doi.org/10.1016/j.tecto.2006.02.011

Kennett, B., Engdahl, E., & Buland, R. (1995). Constraints on seismic velocities in the Earth from travel-times. *Geophysical Journal International*, *122*(1), 108–124. https://doi.org/10.1111/j.1365-246X.1995.tb03540.x

Kim, Y., & Clayton, R. W. (2015). Seismic properties of the Nazca oceanic crust in southern Peruvian subduction system. *Earth and Planetary Science Letters*, *429*, 110–121. https://doi.org/10.1016/j.epsl.2015.07.055

Kim, Y., Clayton, R. W., Asimow, P. D., & Jackson, J. M. (2013). Generation of talc in the mantle wedge and its role in subduction dynamics in central Mexico. *Earth and Planetary Science Letters*, *384*, 81–87. https://doi.org/10.1016/j.epsl.2013.10.006

Kim, Y., Clayton, R. W., & Jackson, J. M. (2010). Geometry and seismic properties of the subducting Cocos plate in central Mexico. *Journal of Geophysical Research*, *115*(B6), B06310. https://doi.org/10.1029/2009JB006942

Király, Á., Portner, D. E., Haynie, K. L., Chilson-Parks, B. H., Ghosh, T., Jadamec, M., et al. (2020). The effect of slab gaps on subduction dynamics and mantle upwelling. *Tectonophysics*, *785*, 228458. https://doi.org/10.1016/j.tecto.2020.228458

Lee, H., Bezada, M. J., & Faccenda, M. (2021). Can sub-slab low-velocity anomalies be an artifact caused by anisotropy? A case study from the Alboran slab area in the western Mediterranean. *Tectonophysics*, *819*, 229080. https://doi.org/10.1016/j.tecto.2021.229080

Lee, H., Bezada, M. J., & Kim, Y. (2022). The origin of the low-velocity anomalies beneath the rootless Atlas Mountains: Insights gained from modeling of anisotropy developed by the travel of canary plume. *Journal of Geophysical Research: Solid Earth*, *127*(11), e2022JB024622. https://doi.org/10.1029/2022JB024622

Lee, H., Kim, Y., Bezada, M. J., & Clayton, R. W. (2023). The dV_P/V_P of our prescribed anisotropy tomography model [Dataset]. Zenodo. https://doi.org/10.5281/zenodo.10068064

Lim, H., Kim, Y., Clayton, R. W., & Thurber, C. H. (2018). Seismicity and structure of Nazca Plate subduction zone in southern Peru. *Earth and Planetary Science Letters*, *498*, 334–347. https://doi.org/10.1016/j.epsl.2018.07.014

Lloyd, S. M., & Van der Lee, S. (2008). Influence of observed mantle anisotropy on isotropic tomographic models. *Geochemistry, Geophysics, Geosystems*, *9*(7), Q07007. https://doi.org/10.1029/2008GC001997

Long, M. D. (2016). The Cascadia Paradox: Mantle flow and slab fragmentation in the Cascadia subduction system. *Journal of Geodynamics*, *102*, 151–170. https://doi.org/10.1016/j.jog.2016.09.006

Long, M. D., & Becker, T. W. (2010). Mantle dynamics and seismic anisotropy. *Earth and Planetary Science Letters*, *297*(3–4), 341–354. https://doi.org/10.1016/j.epsl.2010.06.036

Long, M. D., Biryol, C. B., Eakin, C. M., Beck, S. L., Wagner, L. S., Zandt, G., et al. (2016). Overriding plate, mantle wedge, slab, and subslab contributions to seismic anisotropy beneath the northern Central Andean Plateau [Dataset]. Geochemistry, Geophysics, Geosystems, *17*(7), 2556–2575. https://doi.org/10.1002/2016GC006316

Lynner, C., & Beck, S. L. (2020). Subduction dynamics and structural controls on shear wave splitting along the South American convergent margin [Dataset]. Journal of South American Earth Sciences, *104*, 102824. https://doi.org/10.1016/j.jsames.2020.102824

Ma, Y., & Clayton, R. W. (2015). Flat slab deformation caused by interplate suction force. *Geophysical Research Letters*, *42*(17), 7064–7072. https://doi.org/10.1002/2015GL065195

Manea, V., & Gurnis, M. (2007). Subduction zone evolution and low viscosity wedges and channels. *Earth and Planetary Science Letters*, *264*(1), 22–45. https://doi.org/10.1016/j.epsl.2007.08.030

Manea, V. C., Manea, M., Ferrari, L., Orozco-Esquivel, T., Valenzuela, R. W., Husker, A., & Kostoglodov, V. (2017). A review of the geodynamic evolution of flat slab subduction in Mexico, Peru, and Chile. *Tectonophysics*, *695*, 27–52. https://doi.org/10.1016/j.tecto.2016.11.037

Manea, V. C., Pérez-Gussinyé, M., & Manea, M. (2012). Chilean flat slab subduction controlled by overriding plate thickness and trench rollback. *Geology*, *40*(1), 35–38. https://doi.org/10.1130/G32543.1

Martinod, J., Funiciello, F., Faccenna, C., Labanieh, S., & Regard, V. (2005). Dynamical effects of subducting ridges: Insights from 3-D laboratory models. *Geophysical Journal International*, *163*(3), 1137–1150. https://doi.org/10.1111/j.1365-246X.2005.02797.x

McKenzie, D., & O'Nions, R. K. (1991). Partial melt distributions from inversion of rare Earth Element concentrations. *Journal of Petrology*, *32*(5), 1021–1091. https://doi.org/10.1093/petrology/32.5.1021

Menke, W. (2015). Equivalent heterogeneity analysis as a tool for understanding the resolving power of anisotropic travel-time tomography. *Bulletin of the Seismological Society of America*, *105*(2A), 719–733. https://doi.org/10.1785/0120140150

Myers, E. K., Roland, E. C., Tréhu, A. M., Davenport, K., & the PICTURES Group. (2022). Crustal structure of the incoming Iquique Ridge offshore Northern Chile. *Journal of Geophysical Research: Solid Earth*, *127*(2), e2021JB023169. https://doi.org/10.1029/2021JB023169

Norabuena, E., Leffler-Griffin, L., Mao, A., Dixon, T., Stein, S., Sacks, I. S., et al. (1998). Space geodetic observations of Nazca-South America convergence across the central Andes. *Science*, *279*(5349), 358–362. https://doi.org/10.1126/science.279.5349.358

Pilger, R. H., Jr. (1981). Plate reconstructions, aseismic ridges, and low-angle subduction beneath the Andes. *GSA Bulletin*, *92*(7), 448–456. https://doi.org/10.1130/0016-7606(1981)92<448:PRARAL>2.0.CO;2

Pilger, R. H., Jr., & Handschumacher, D. W. (1981). The fixed-hotspot hypothesis and origin of the Easter—Sala y Gomez—Nazca trace. *GSA Bulletin*, *92*(7), 437–446. https://doi.org/10.1130/0016-7606(1981)92<437:TFHAOO>2.0.CO;2

Polet, J., Silver, P. G., Beck, S., Wallace, T., Zandt, G., Ruppert, S., et al. (2000). Shear wave anisotropy beneath the Andes from the BANJO, SEDA, and PISCO experiments [Dataset]. Journal of Geophysical Research, *105*(B3), 6287–6304. https://doi.org/10.1029/1999JB900326

Portner, D. E., Beck, S., Zandt, G., & Scire, A. (2017). The nature of subslab slow velocity anomalies beneath South America. *Geophysical Research Letters*, *44*(10), 4747–4755. https://doi.org/10.1002/2017GL073106

Portner, D. E., Rodríguez, E. E., Beck, S., Zandt, G., Scire, A., Rocha, M. P., et al. (2020). Detailed structure of the subducted Nazca slab into the lower mantle derived from continent-scale teleseismic *P* wave tomography. *Journal of Geophysical Research: Solid Earth*, *125*(5), e2019JB017884. https://doi.org/10.1029/2019JB017884

Protti, M., Gïendel, F., & McNally, K. (1995). Correlation between the age of the subducting Cocos plate and the geometry of the Wadati-Benioff zone under Nicaragua and Costa Rica. In P. Mann (Ed.), *Geologic and Tectonic Development of the Caribbean Plate Boundary in Southern Central America* (Vol. 295). Geological Society of America. https://doi.org/10.1130/SPE295-p309

Putirka, K. D. (2005). Mantle potential temperatures at Hawaii, Iceland, and the mid-ocean ridge system, as inferred from olivine phenocrysts: Evidence for thermally driven mantle plumes. *Geochemistry, Geophysics, Geosystems*, *6*(5). https://doi.org/10.1029/2005GC000915

Reiss, M. C., Rümpker, G., & Wölbern, I. (2018). Large-scale trench-normal mantle flow beneath central South America [Dataset]. Earth and Planetary Science Letters, *482*, 115–125. https://doi.org/10.1016/j.epsl.2017.11.002

Rodríguez, E. E., Portner, D. E., Beck, S. L., Rocha, M. P., Bianchi, M. B., Assumpção, M., et al. (2021). Mantle dynamics of the Andean subduction zone from continent-scale teleseismic S-wave tomography. *Geophysical Journal International*, *224*(3), 1553–1571. https://doi.org/10.1093/gji/ggaa536

Russo, R. M., & Silver, P. G. (1994). Trench-parallel flow beneath the Nazca Plate from seismic anisotropy. *Science*, *263*(5150), 1105–1111. https://doi.org/10.1126/science.263.5150.1105

Ryan, J., Beck, S., Zandt, G., Wagner, L., Minaya, E., & Tavera, H. (2016). Central Andean crustal structure from receiver function analysis. *Tectonophysics*, *682*, 120–133. https://doi.org/10.1016/j.tecto.2016.04.048

Savage, M. K. (1999). Seismic anisotropy and mantle deformation: What have we learned from shear wave splitting? *Reviews of Geophysics*, *37*(1), 65–106. https://doi.org/10.1029/98RG02075

Schellart, W. P. (2020). Control of subduction zone age and size on flat slab subduction. *Frontiers in Earth Science*, *8*. https://doi.org/10.3389/feart.2020.00026

Schilling, J.-G. (1991). Fluxes and excess temperatures of mantle plumes inferred from their interaction with migrating mid-ocean ridges. *Nature*, *352*(6334), 397–403. https://doi.org/10.1038/352397a0

Schmandt, B., & Humphreys, E. (2010). Complex subduction and small-scale convection revealed by body-wave tomography of the western United States upper mantle. *Earth and Planetary Science Letters*, *297*(3), 435–445. https://doi.org/10.1016/j.epsl.2010.06.047

Scire, A., Biryol, C. B., Zandt, G., & Beck, S. (2015). Imaging the Nazca slab and surrounding mantle to 700 km depth beneath the central Andes (18°S to 28°S). *Memoir of the Geological Society of America*, 23–41. https://doi.org/10.1130/2015.1212(02)

Scire, A., Zandt, G., Beck, S., Long, M., Wagner, L., Minaya, E., & Tavera, H. (2016). Imaging the transition from flat to normal subduction: Variations in the structure of the Nazca slab and upper mantle under southern Peru and northwestern Bolivia. *Geophysical Journal International*, *204*(1), 457–479. https://doi.org/10.1093/gji/ggv452

Skinner, S. M., & Clayton, R. W. (2013). The lack of correlation between flat slabs and bathymetric impactors in South America. *Earth and Planetary Science Letters*, *371–372*, 1–5. https://doi.org/10.1016/j.epsl.2013.04.013

Sobolev, S. V., Grésillaud, A., & Cara, M. (1999). How robust is isotropic delay time tomography for anisotropic mantle? *Geophysical Research Letters*, *26*(4), 509–512. https://doi.org/10.1029/1998GL900206

Suchoy, L., Goes, S., Chen, F., & Davies, D. R. (2022). How aseismic ridges modify the dynamics of free subduction: A 3-D numerical investigation. *Frontiers in Earth Science*, *10*. https://doi.org/10.3389/feart.2022.852742

Syracuse, E. M., & Abers, G. A. (2006). Global compilation of variations in slab depth beneath arc volcanoes and implications. *Geochemistry, Geophysics, Geosystems*, *7*(5), Q05017. https://doi.org/10.1029/2005GC001045

Toomey, D. R., & Blue Tech Seismics, Inc. (2012). July, 2012 Release [Software]. Stingray/TomoLab. Retrieved from https://pages.uoregon.edu/drt/Stingray/pages/89.html

Toomey, D. R., Solomon, S. C., & Purdy, G. M. (1994). Tomographic imaging of the shallow crustal structure of the East Pacific Rise at 9°30′N. *Journal of Geophysical Research*, *99*(B12), 24135–24157. https://doi.org/10.1029/94JB01942

VanDecar, J. C., & Crosson, R. S. (1990). Determination of teleseismic relative phase arrival times using multi-channel cross-correlation and least squares. *Bulletin of the Seismological Society of America*, *80*(1), 150–169.

VanderBeek, B. P., & Faccenda, M. (2021). Imaging upper mantle anisotropy with teleseismic P-wave delays: Insights from tomographic reconstructions of subduction simulations. *Geophysical Journal International*, *225*(3), 2097–2119. https://doi.org/10.1093/gji/ggab081

van Hunen, J., van den Berg, A. P., & Vlaar, N. J. (2004). Various mechanisms to induce present-day shallow flat subduction and implications for the younger Earth: A numerical parameter study. *Physics of the Earth and Planetary Interiors*, *146*(1), 179–194. https://doi.org/10.1016/j.pepi.2003.07.027

Wang, J., & Zhao, D. (2012). P wave anisotropic tomography of the Nankai subduction zone in Southwest Japan. *Geochemistry, Geophysics, Geosystems*, *13*(5), Q05017. https://doi.org/10.1029/2012GC004081

Ward, K. M., Porter, R. C., Zandt, G., Beck, S. L., Wagner, L. S., Minaya, E., & Tavera, H. (2013). Ambient noise tomography across the central Andes [Dataset]. Geophysical Journal International, *194*(3), 1559–1573. https://doi.org/10.1093/gji/ggt166

Ward, K. M., Zandt, G., Beck, S. L., Wagner, L. S., & Tavera, H. (2016). Lithospheric structure beneath the northern Central Andean Plateau from the joint inversion of ambient noise and earthquake-generated surface waves. *Journal of Geophysical Research: Solid Earth*, *121*(11), 8217–8238. https://doi.org/10.1002/2016JB013237

Woods, M. T., & Okal, E. A. (1994). The structure of the Nazca ridge and Sala y Gomez seamount chain from the dispersion of Rayleigh waves. *Geophysical Journal International*, *117*(1), 205–222. https://doi.org/10.1111/j.1365-246X.1994.tb03313.x

Zhang, S., & Karato, S. (1995). Lattice preferred orientation of olivine aggregates deformed in simple shear. *Nature*, *375*(6534), 774–777. https://doi.org/10.1038/375774a0

Zhao, D., Yu, S., & Liu, X. (2016). Seismic anisotropy tomography: New insight into subduction dynamics. *Gondwana Research*, *33*, 24–43. https://doi.org/10.1016/j.gr.2015.05.008